Catalysis Letters (2024) 154:23–33
https://doi.org/10.1007/s10562-023-04293-3

Cobalt Pyrophosphate Nanosheets Effectively Boost Photoelectrochemical Water Splitting Efficiency of $BiVO_4$ Photoanodes

Xiang Wen[1] · Guyu Zhou[1] · Jikai Liu[1]

Received: 2 November 2022 / Accepted: 26 January 2023 / Published online: 13 February 2023
© The Author(s), under exclusive licence to Springer Science+Business Media, LLC, part of Springer Nature 2023

Abstract

Photoanodes are a critical part of the photoelectrochemical (PEC) water splitting technology that drives the conversion of solar energy to hydrogen, while bismuth vanadate ($BiVO_4$) is one of the most promising photoanode materials available. Here, we provide a simple spin-coating method to modify the PEC performance of $BiVO_4$ by coating ultrathin cobalt pyrophosphate ($Co_2P_2O_7$) nanosheets as a co-catalyst layer onto the surface of $BiVO_4$. The $Co_2P_2O_7/BiVO_4$ composite photoanode achieved a photocurrent density of 3.93 mA cm^{-2} at 1.23 V versus RHE, which is 2.5 times higher than bare $BiVO_4$ and considerably better than Co-Pi/$BiVO_4$ and $CoO_x/BiVO_4$, with an improved charge injection efficiency of 71%. The key to the substantial enhancement of PEC performance is that $Co_2P_2O_7$ nanosheets accelerate the charge transfer process all over the $BiVO_4$ surface, not only as a water oxidation catalyst (OEC) layer accelerating the kinetic rate of the oxygen evolution reaction (OER) at the junction with the water, but also suppressing the rate of photogenerated electron–hole recombination at the $Co_2P_2O_7/BiVO_4$ junction. A potential mechanism for the enhanced PEC performance of $Co_2P_2O_7$ nanosheets is proposed, and this work provides assistance in the design of transition metal pyrophosphate, cobalt-based nanomaterial morphologies to enhance the PEC properties of $BiVO_4$.

Graphical Abstract

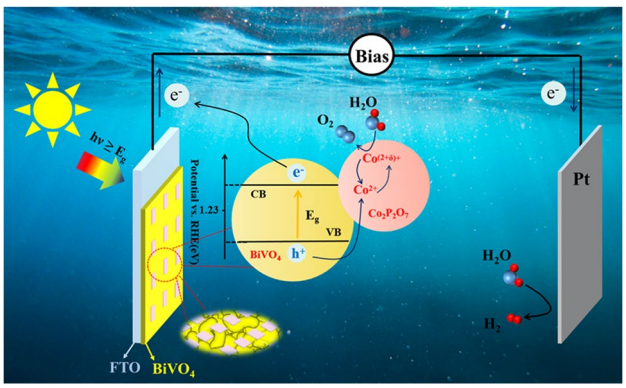

Keywords $BiVO_4$ · Photoanode · Co-catalyst · OER, · $Co_2P_2O_7$, · PEC

1 Introduction

The use of visible light responsive semiconductors for hydrogen production by photoelectrochemical (PEC) water splitting is considered to be one of the attractive technologies for hydrogen energy in the future [1]. Although the photocathode directly participates in the Hydrogen evolution

✉ Jikai Liu
jikailiu@xtu.edu.cn

[1] School of Chemical Engineering, Xiangtan University, Xiangtan 411105, People's Republic of China

reaction, the photoanode is often the key reason of limiting the high hydrogen production efficiency of the solar water splitting cells due to its more complex mechanism of the oxygen evolution semi-reaction [2, 3]. The common photoanodes available today are generally n-type semiconductors and come in a wide variety, including $BiVO_4$ [4, 5], WO_3 [6, 7], Ta_3N_5 [8, 9], α-Fe_2O_3 [10, 11], etc. Among which them, $BiVO_4$ is a vigorous research topic of photoanode in the field of PEC water splitting due to its advantages, such as its appropriate band gap, sufficiently positive valence band position for electrochemical potential of oxygen evolution reaction (OER) of water splitting, high theoretical photocurrent density, etc. [12].However, the PEC activity of $BiVO_4$ is greatly limited by photon absorption capacity, severe photogenerated electron–hole recombination in bulk phases & interfaces, and the slow OER rate [13, 14] caused by direct contact with water when $BiVO_4$ is used as a photoanode for water oxidation under sunlight [15]. Therefore, the methods such as element doping [16, 17], increasing the oxygen vacancies (O_v) in the bulk phase or on the surface of $BiVO_4$ [18–20], construction of heterojunctions [21, 22], loading of transition-metal-based co-catalysts [13, 23–25], etc., have been developed to solve the corresponding problems. A significant portion of the co-catalyst loading is in the form of an oxygen evolution reaction catalyst (OEC) layer catalyzing the kinetics of water oxidation [12], which is one of the most commonly used methods to enhance the PEC performance of $BiVO_4$. Choi et al. expatiated that amorphous NiOOH can act as the OEC layer to accelerate the water oxidation kinetics at the NiOOH/solution junction, while amorphous FeOOH has weaker water oxidation activity than amorphous NiOOH and more importantly inhibits the electron–hole recombination at the FeOOH/$BiVO_4$ junction [13].

Ultrathin two-dimensional transition metal nanomaterials generally refer to the transition metal element-containing materials with the plane span of more than 100 nm and a thickness of less than a few nanometers [26]. Many of the materials have been used as cocatalysts on the surface of $BiVO_4$, such as Mxene [27–29], Layered Double Hydroxides (LDHs) [30, 31], MoS_2 [32], etc. Such materials always have high transparency, expose the transition metal sites with high distribution density, and enable the carriers to undergo weaker interlayer interactions during transport, so they are very suitable for some OECs that rely on transition metal active centres for catalysis, having better carrier mobility than bulk cocatalysts, and reducing the occurrence of more carrier recombination centres in the pathway prior to participation in the OER [26, 28, 33, 34].

Cobalt-based co-catalysts have been extensively developed to enhance the photoelectrochemical properties of water oxidation with $BiVO_4$, such as Co-MOF [25], Co-Pi [23], CoOOH [35], etc. Cobalt pyrophosphate ($Co_2P_2O_7$) has emerged in recent years as a water oxidation catalyst containing two PO_3 groups coordinated to an O atom to form a flexible pyrophosphate group. Pyrophosphate groups can be rotated to form additional Co–O bonds to stabilise the easily reconstructed five-coordinated cobalt, resulting in a more efficient cobalt valence change when participating in the OER of water splitting [36]. So far various nanomorphs of $Co_2P_2O_7$ have been used to catalyse OER of water splitting, such as coralline [37], needle [38] and ultrathin sheets [39]. Although cobalt pyrophosphate has shown promise in replacing noble metal-based catalysts for inexpensive and efficient use to catalyze water oxidation, research on its application to PEC water splitting is scarce.

Based on the above background, we report for the first time a highly efficient composite photoanode material consisting of ultrathin cobalt pyrophosphate nanosheets and $BiVO_4$. The nanoscale worm-like $BiVO_4$ photoanode was successfully coated with $Co_2P_2O_7$ nanosheets as a co-catalyst layer to participate in the photoelectrochemical water oxidation using a simple spin-coating and annealing process. Not surprisingly, $Co_2P_2O_7$/$BiVO_4$ achieves substantially enhanced PEC properties compared to bare $BiVO_4$, with a photocurrent density of 3.93 mA cm^{-2} (1.23 V vs. RHE) measured under AM 1.5G illumination and in 1 M potassium borate solution (pH = 9.3), which outperforms conventional Co-Pi, CoO_x catalysts. At the same time, $Co_2P_2O_7$/$BiVO_4$ has a high photoelectric conversion efficiency, with an IPCE value of 58.7% at 430 nm. The $Co_2P_2O_7$ nanosheets not only act as an OEC layer to enhance the charge injection efficiency of the electrolyte but also improve the efficiency of photogenerated carrier transport and separation at the interface and potentially act as a hole storage layer. This work provides a new broadening of the design of cobalt-based cocatalysts for the enhancement of PEC properties of $BiVO_4$.

2 Experimental Section

2.1 Materials and Chemicals

P-benzoquinone ($C_8H_6O_4$), bismuth nitrate pentahydrate ($Bi(NO_3)_3{\cdot}5H_2O$), cobalt acetate tetrahydrate ($Co(AC)_2{\cdot}4H_2O$), vanadium pentoxide ($C_{10}H_{14}O_5V$), dimethyl sulfoxide (C_2H_6SO), sodium pyrophosphate ($Na_4P_2O_7$), vanadium acetylacetonate oxide ($C_{10}H_{14}O_5V$) are analytically pure and purchased from Aladdin. Potassium iodide (KI, AR), nitric acid (HNO_3, 26–28 wt.%), ethanol (C_2H_6O, AR), potassium hydroxide (NaOH, 97%) were purchased from Sinopharm. All reagents can be used directly without purification. DI water (resistivity 18.25 MΩ cm) was used for the reactions and PEC measurements. FTO (F-SnO_2) substrates (1 × 2 cm^2, resistance < 14 Ω/cm^2) were purchased from Nippon Sheet Glass and cleaned by ultrasonication

with acetone, ethanol and DI water respectively for 10 min before use.

2.2 Synthesis of $Co_2P_2O_7/BiVO_4$ Film, $Co_2P_2O_7$ Nanosheets

The synthesis of $BiVO_4$ film was based on a previously reported method (Supporting Information) [13]. 1.0 g of $Na_4P_2O_7$ and 1.0 g of $Co(AC)_2{\cdot}4H_2O$ were added to 20 ml of DI water and stirred until homogeneous, then transferred to 25 ml of Teflon container and reacted at 160 °C for 8 h. The product was repeatedly cleaned with deionized water and ethanol, dried under vacuum at 60 °C for 24 h, then prepared into ethanol solution (0.7 mg/ml) and treated with ultrasound for 1 h. The $BiVO_4$ photoanode was placed in a spin coater and 50 µl of the above solution was added dropwise to the surface of the $BiVO_4$ film and then spin coated at 2000 rpm for 20 s. The process was repeated four times. Finally, the finished film was annealed in a tube furnace at 300 °C for 30 min under argon flow atmosphere (ramp rate = 5 °C/min) to obtain $Co_2P_2O_7/BiVO_4$ film. Individual $Co_2P_2O_7$ nanosheets were prepared by the same procedure but only containing hydrothermal and annealing.

2.3 Synthesis of $CoO_x/BiVO_4$, Co-Pi/$BiVO_4$ Film

Based on reported methods as detailed in the Supporting Information [23, 40].

2.4 Characterization

X-ray powder diffraction (XRD, Cu-Kα radiation, U_1tima IV) for crystallographic analysis, Raman spectroscopy (LabRAM Evolution, excitation wavelength = 532 nm) for structural analysis. The scanning electron microscopy (SEM, Zeiss-Supra 55, accelerating voltage 10 kV) is equipped with Energy Dispersive X-Ray Spectroscopy (EDX), X-ray photoelectron spectroscopy (XPS, Thermo ESCALAB 250XI) and atomic force microscopy (AFM, Bruker Dimension Icon) are used for morphological observations and elemental analysis. UV–Vis diffuse reflectance spectroscopy (UV-2550 Shimadzu) is used to measure visible absorbance.

2.5 PEC Measurement

All PEC measurements were carried out in an electrochemical workstation (VersaSTAT 3). The standard three-electrode system uses a 1 M potassium borate (KBi, pH = 9.3) solution as the electrolyte, a Pt sheet as the counter electrode, an Ag/AgCl electrode (3.5 M KCl) as the reference electrode ($E_{RHE} = E_{Ag/AgCl} + 0.1976\ V + 0.0591 \times pH$, 25 °C) and a photoanode as the working electrode. A 300 W xenon lamp (Newport Corp.) with an AM 1.5G filter was used to provide a simulated solar intensity of 100 $mW{\cdot}cm^{-2}$ (illuminated from the back of the FTO). Linear sweep voltammetry (LSV) and transient response under chopped light were scanned at a rate of 10 $mV{\cdot}s^{-1}$. Electrochemical impedance spectroscopy (EIS) measurements were carried out under AM 1.5 G illumination and set with a DC bias of 1.0 V vs. RHE (frequency range: 0.01 Hz to 100 kHz). Mott-Schottky (MS) curves (frequency: 1 kHz) were obtained by setting 10mv increments in the voltage range from 0.1 to 0.6 V in the dark.

2.6 Determination of Photoelectric Efficiency

The incidence photon to current efficiency (IPCE) at each visible wavelength is obtained using 300 W xenon lamps with monochromators and can be calculated using the following equation:

$$\mathrm{IPCE}\ (\%) = \frac{1240 \times J_\lambda}{\lambda \times \mathrm{P}} \times 100\%$$

where λ is the wavelength of monochromatic light (nm), J_λ ($mA{\cdot}cm^{-2}$, 1.23 V vs. RHE) is the photocurrent density measured at a wavelength of λ, and P is the total light intensity (100 $mW{\cdot}cm^{-2}$).

The charge injection efficiency (η_{in}) and the charge separation efficiency (η_{sep}) are calculated as follows:

$$\eta_{in}(\%) = J_{H_2O} \big/ J_{sulfite}$$

$$\eta_{sep}(\%) = J_{sulfite} \big/ J_{abs}$$

where J_{H_2O} and $J_{sulfite}$ are the photocurrent densities ($mA{\cdot}cm^{-2}$, at the same bias voltage) measured for the photoanode in KBi buffer versus KBi buffer containing 1 M Na_2SO_3, respectively. J_{abs} ($mA{\cdot}cm^{-2}$) can be integrated by the following equation:

$$J_{abs} = \int N_{ph}(\lambda) \times \left(1 - 10^{-A_{(\lambda)}}\right) \times \mathrm{e} \times \mathrm{d}\lambda$$

where $N_{ph}(\lambda)$ and $A_{(\lambda)}$ are the photon flux ($mW{\cdot}cm^{-2}{\cdot}nm^{-1}$) and absorbance at wavelength λ ($1240/\lambda \geq E_g$) in the simulated solar spectrum (AM 1.5 G), respectively. E_g (eV) is the band gap value of the photoanode and e is the charge of the electron.

Applied bias photon to current efficiency (ABPE) can be calculated by the following equation:

$$\mathrm{ABPE}(\%) = \frac{\left(1.23 - V_b\right) \times J_{H_2O}}{\mathrm{P}}$$

where V_b is the applied bias voltage (vs. RHE) when the photocurrent density is J_{H_2O} under simulated sunlight (AM 1.5 G).

3 Results and Discussion

The synthesis of $Co_2P_2O_7/BiVO_4$ composite photoanodes is shown in Scheme 1. BiOI nanosheet film grown by electrodeposition on FTO [13] was reacted with a vanadium source (VO (acac) $_2$) to produce $BiVO_4$ films. At the same time, a solution containing cobalt ions with sodium pyrophosphate was hydrothermally treated. Finally, ethanol solutions of the hydrothermal products (0.3, 0.7, 1.1 mg/ml) were spin-coated onto the $BiVO_4$ films and annealed under argon to obtain the final $Co_2P_2O_7/BiVO_4$ films.

The crystalline phase structures of the prepared $Co_2P_2O_7/BiVO_4$, $BiVO_4$, and $Co_2P_2O_7$ were analysed using XRD. As shown in Fig. 1a, excluding the diffraction peaks corresponding to the FTO (F:SnO_2) substrate, the intense peak signals of the prepared $BiVO_4$ films at 2θ of 19.07°, 29.05°, 30.66°, 35.34° can be indexed to the typical characteristic peaks of monoclinic scheelite $BiVO_4$ (JCPDS No. 14–0688) [41]. Meanwhile, the sharp peaks of $Co_2P_2O_7$ at 2θ = 29.18°, 30.09°, 34.65° can be indexed to the (1 2 0), (1 0 2), (0 3 1) crystal planes of $Co_2P_2O_7$ (JCPDS No. 82–0521) [39]. The XRD patterns of $Co_2P_2O_7/BiVO_4$ in overall did not show the presence of $Co_2P_2O_7$ diffraction peak distribution, which may be due to the low relative loading of $Co_2P_2O_7$ at the detection depth of XRD. In order to demonstrate more conclusively the presence of pyrophosphate groups in the synthesised $Co_2P_2O_7$, $Co_2P_2O_7/BiVO_4$, Raman spectroscopic analysis was used. The Raman spectra of $Co_2P_2O_7$ are presented in Fig. S1. The characteristic peaks at 1043 and 734 cm^{-1} correspond to the symmetric vibrations of the PO_3 group and POP bridge, respectively, and the peaks at 453 and 351 cm^{-1} are attributed to the rocking of PO_3 modes and POP bridge deformation, respectively [38]. Also as shown in Fig. 1b, $Co_2P_2O_7/BiVO_4$ fails to show the typical characteristic peaks of $Co_2P_2O_7$ described above, while the strong peaks at 126, 211, 366, and 827 cm^{-1} are attributed to the characteristic Raman peaks of monoclinic $BiVO_4$ [42].

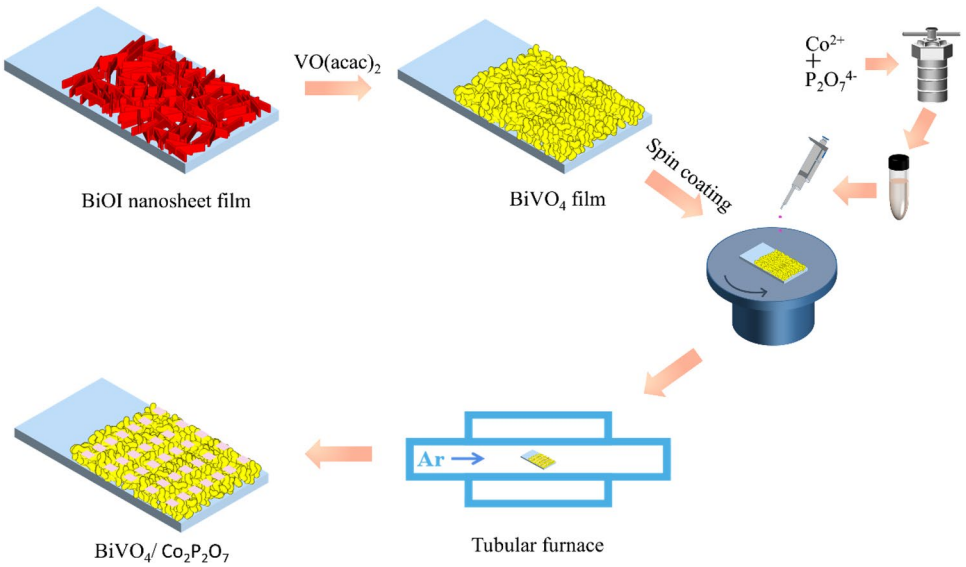

Scheme 1 Schematic illustration of the synthesis approach of Co2P2O7/BiVO4 composite photoanode

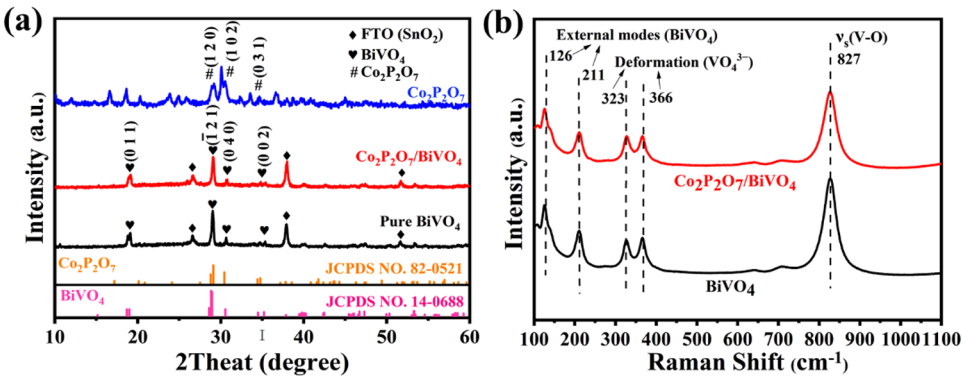

Fig. 1 **a** The XRD patterns of the $BiVO_4$, $Co_2P_2O_7$, $Co_2P_2O_7/BiVO_4$ and **b** Raman spectra of the $BiVO_4$, $Co_2P_2O_7/BiVO_4$

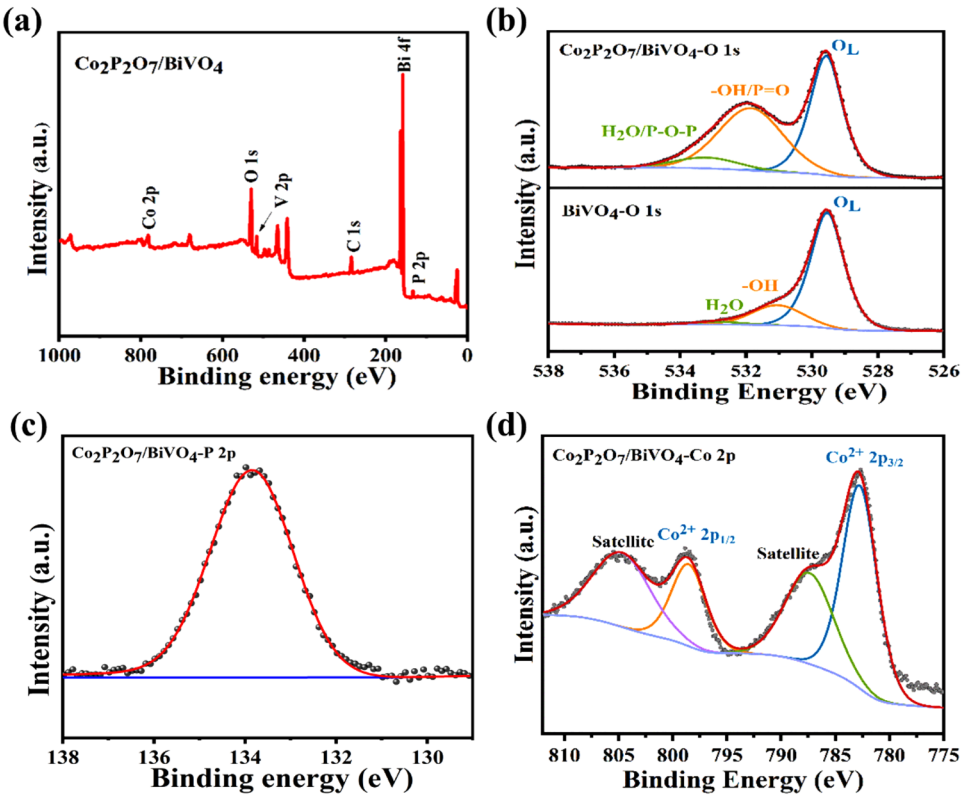

Fig. 2 **a** Full XPS spectrum and high-resolution O 1 s (**b**), P 2p (**c**) and Co 2p (**d**) XPS spectra of the $Co_2P_2O_7/BiVO_4$ photoanode. The O 1 s spectra of the $BiVO_4$ was included in (**b**) for comparison

The surface elements of $Co_2P_2O_7/BiVO_4$ were analysed using XPS. The XPS full spectrum of $Co_2P_2O_7/BiVO_4$ in Fig. 2a shows the presence of Bi, V, O, Co, P. The peaks of Bi 4f and V 2p of $Co_2P_2O_7/BiVO_4$ are shifted relative to $BiVO_4$ (Fig. S2a, b), indicating the interaction of $Co_2P_2O_7$ with $BiVO_4$ [27]. The peaks at $Co_2P_2O_7/BiVO_4$ binding energies of 158.4 eV and 163.6 eV correspond to Bi $4f_{7/2}$ and Bi $4f_{5/2}$, respectively, while the double peaks at 516.3 eV and 523.7 eV correspond to V $2p_{3/2}$ and V $2p_{1/2}$, respectively [43]. The O 1 s spectra of $Co_2P_2O_7$/ $BiVO_4$ and $BiVO_4$ are compared in Fig. 2b. For $BiVO_4$, the peaks at binding energies of 529.5, 531.1 and 532.9 eV can be attributed to lattice oxygen (O_L), chemisorbed/dissociated oxygen and H_2O, respectively [44], and the peak area ratios were 77.8%, 19.5% and 2.7%, respectively. However, the peaks of $Co_2P_2O_7$/ $BiVO_4$ at binding energies of 529.6, 531.8 and 533.2 eV had peak areas ratios of 46.8%, 45.4% and 7.9%, respectively. The increased peak area ratio of the peaks at $Co_2P_2O_7/BiVO_4$ binding energies of 531.8 and 533.2 eV was attributed to P = O and P-O-P, respectively [38]. The symmetric peak for P 2p in Fig. 2c (133.4 eV) can be attributed to the pyrophosphate group in $Co_2P_2O_7$ [38]. The peaks of Co 2p in Fig. 2d can be fitted with peaks at 781.5 eV (Co $2p_{3/2}$), 796.8 eV (Co $2p_{1/2}$) and 786.7, 802.9 eV (shake-up satellites), corresponding to the characteristic peaks of Co (II) [45], which are consistent with the elemental valence characteristics of $Co_2P_2O_7$. Meanwhile, the atomic ratio of Co versus P estimated from the peak area of each element is close to 1:1, which further supports the successful loading of $Co_2P_2O_7$.

The surface morphology of the prepared photoanodes was characterised by SEM. Figure 3a shows a worm-like distribution of $BiVO_4$ with diameters ranging from approximately 100–300 nm on the FTO surface, which is consistent with the reported article [13]. We found that the synthesised $Co_2P_2O_7$ ethanol solution was well dispersed for a certain period of time (several hours), suggesting the ultrathin nature of $Co_2P_2O_7$ [29]. After prolonged sonication, the $Co_2P_2O_7$ solution was spin-coated onto the $BiVO_4$ surface and the SEM image (Fig. 3b) showed the random deposition of $Co_2P_2O_7$ in the form of square nanosheets on the $BiVO_4$ surface. The length of the $Co_2P_2O_7$ nanosheets is slightly larger than the diameter of the $BiVO_4$ particles but still between a few hundred nanometers, which facilitates its embedding in the porous interstices of $BiVO_4$ to promote better contacting with $BiVO_4$. AFM measurements of the synthesised $Co_2P_2O_7$ (Fig. 3c) confirmed the ultrathin character of the nanosheets (~3 nm), which is consistent with the relevant literature [39]. Also, the distribution of Bi, V, O, Co, and P on the $Co_2P_2O_7/BiVO_4$ surface and the mass percentages of each element (Fig. S3) were clearly shown based on X-ray energy dispersion analysis by SEM (Fig. 3d), which deduced an atomic ratio of Co and P of approximately 1:1, echoing the conclusions of the XPS analysis.

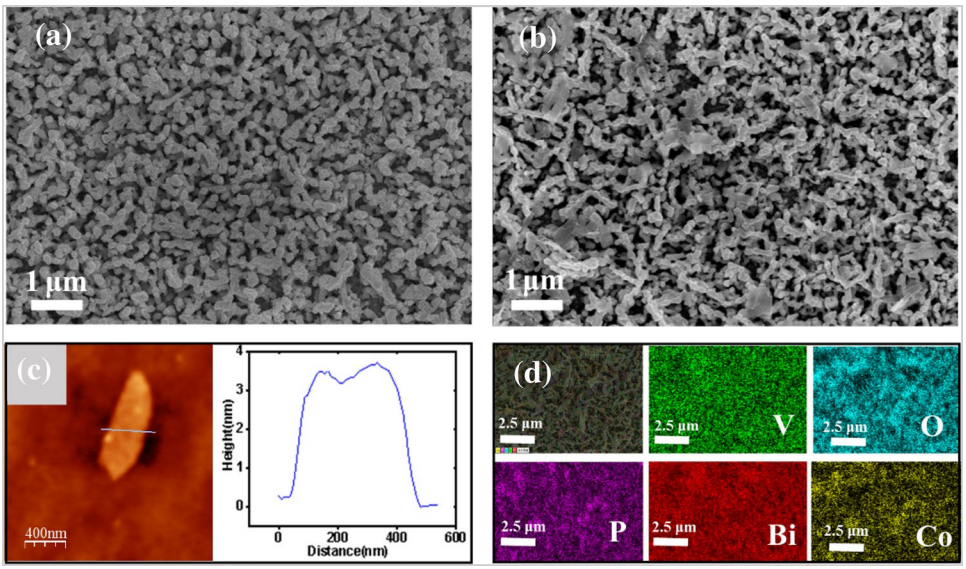

Fig. 3 SEM images of **a** $BiVO_4$, **b** $Co_2P_2O_7/BiVO_4$ and **c** AFM image of $Co_2P_2O_7$ and **d** SEM mapping of $Co_2P_2O_7/BiVO_4$

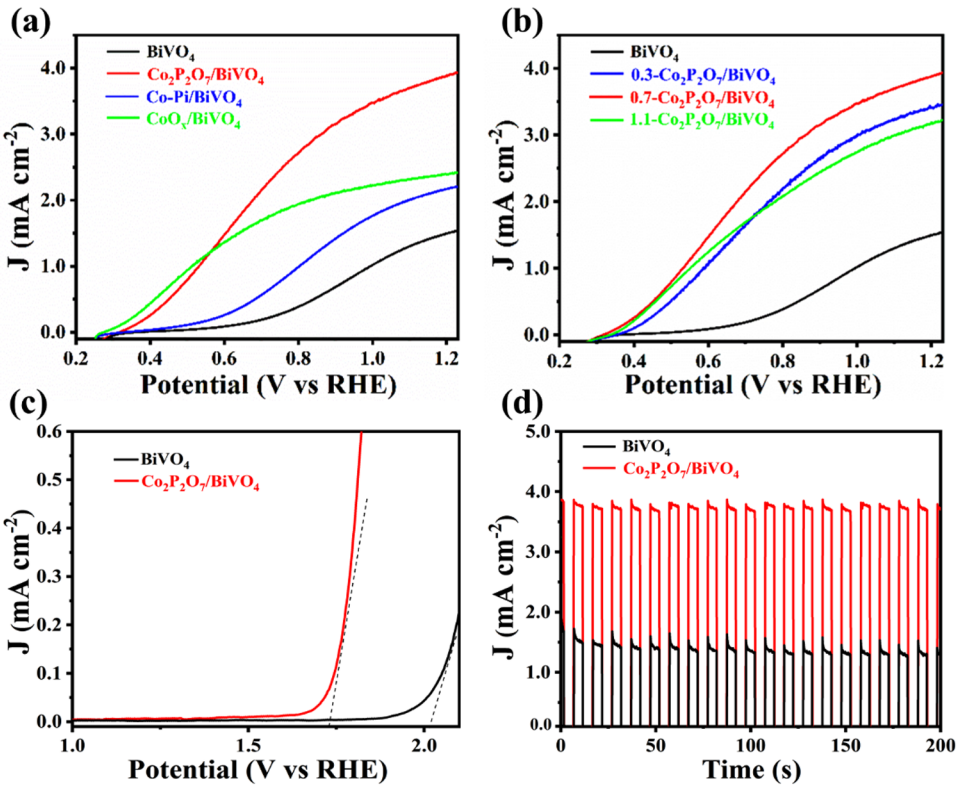

Fig. 4 **a** Linear sweep voltammetry curves of $BiVO_4$, $Co_2P_2O_7/BiVO_4$, Co-Pi/$BiVO_4$, $CoO_x/BiVO_4$ and **b** $Co_2P_2O_7/BiVO_4$ prepared under different spin coating conditions with light irradiation (AM 1.5 G). **c** Linear sweep voltammetry curves of the $BiVO_4$ and $Co_2P_2O_7/BiVO_4$ measured in the dark. **d** Photocurrent density of $BiVO_4$, $Co_2P_2O_7/BiVO_4$ under chopping irradiation

To evaluate the influence of ultrathin $Co_2P_2O_7$ nanosheets on the visible absorption of $BiVO_4$, UV–vis DRS spectra of $Co_2P_2O_7/BiVO_4$ photoanodes prepared under spin-coating with different concentrations of $Co_2P_2O_7$ solution were collected (Fig. S4a). The results show that the absorption band of these photoanodes is around 490 nm and has comparable absorbance in the visible range, indicating that the low loading of $Co_2P_2O_7$ nanosheets has little impact on the visible absorption of $BiVO_4$. A Kubelka–Munk function conversion of the UV–vis DRS spectra was then performed, and the band gap value of the $BiVO_4$ photoanodes was estimated to be approximately 2.45 eV (Fig. S4b), which is consistent with a previous report [17].

The PEC water splitting properties of the $Co_2P_2O_7/BiVO_4$ photoanodes were measured in 1 M potassium borate buffer (pH = 9.3) and under simulated solar illumination (AM 1.5G). Figure 4a shows the Linear sweep voltammetry (LSV) curves of the prepared series of photoanodes, bare $BiVO_4$ has a photocurrent density of merely 1.51 mA cm^{-2} at 1.23 V vs. RHE, which increases to 3.93 mA cm^{-2} (2.5 times) after coating $Co_2P_2O_7$ nanosheets and is significantly higher than Co-Pi/$BiVO_4$ (2.13 mA cm^{-2}) and $CoO_x/BiVO_4$ (2.42 mA cm^{-2}), demonstrating the structural advantages of $Co_2P_2O_7$ ultrathin nanosheets. Figure 4b shows that the influence of the coating of $Co_2P_2O_7$ nanosheets on the photocurrent density of $BiVO_4$ is also evident. The highest photocurrent density of $Co_2P_2O_7/BiVO_4$ is achieved when the concentration of spin-coated $Co_2P_2O_7$ solution is 0.7 mg/ml. Combined with the SEM images of the $BiVO_4$ surface at different $Co_2P_2O_7$ nanosheets loadings in Fig. S5a, b, it can be speculated that at concentrations as low as 0.3 mg/ml, the $Co_2P_2O_7$ nanosheets on the $BiVO_4$ surface are unable to cover a large enough area to assist in the PEC water oxidation. While at concentrations as high as 1.1 mg/ml, we found that as the concentration of the solution increases, the shorter it takes for the $Co_2P_2O_7$ nanosheets in solution to precipitate and aggregate. Abundant $Co_2P_2O_7$ nanosheets meanwhile are more easily aggregated on the surface of $BiVO_4$, thus generating more charge recombination centers and reducing their own water oxidation activity [21]. The LSV curves of the photoanodes measured in the dark are shown in Fig. 4c. The $BiVO_4$/FTO electrode showed a significant negative shift in the onset potential after coating the nanosheets and was able to achieve a steep water oxidation current climb with a very small overpotential compared to the $BiVO_4$/FTO electrode. This reveals that $Co_2P_2O_7$ nanosheets not only have a powerful catalytic activity for photoanodic water oxidation, but also can be used as an excellent OER co-catalyst for water electrolysis. Subsequently, Fig. 4d as well as Fig. S6 show the chopped-light chronoamperometry and the chopping photocurrent density–voltage image of the prepared photoanodes, respectively. When the xenon lamp is switched on, the rapid generation of photogenerated electron–hole pairs at the $BiVO_4$ photoanode causes a strong photocurrent density response, while the subsequent slow OER kinetics and surface accumulation and recombination of photogenerated carriers cause a sudden decrease in photocurrent density resulting in a sharp peak in the current density measurement curve at the moment of sudden illumination [46]. The coating of $Co_2P_2O_7$ nanosheets alleviates this process, and the sharp peaks in the I-t curve of $Co_2P_2O_7/BiVO_4$ due to sudden illumination become slightly flatter compared with $BiVO_4$.

In the subsequent electrochemical impedance spectroscopy (EIS) measurements (Fig. 5a), the arc radius of Nyquist plots for $Co_2P_2O_7/BiVO_4$ becomes very small compared with $BiVO_4$, implying a dramatic reduction in the interfacial

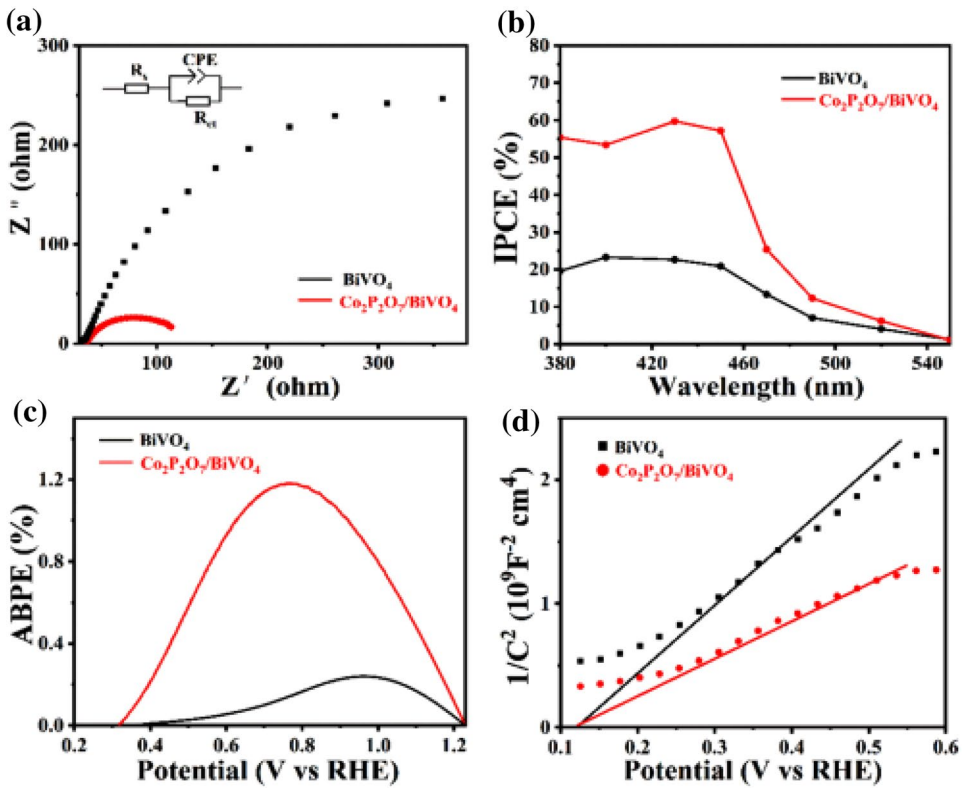

Fig. 5 **a** Nyquist plots of EIS in $BiVO_4$, $Co_2P_2O_7/BiVO_4$ recorded at 1.0 V (vs. RHE) under light irradiation (AM 1.5 G). **b** IPCE and **c** ABPE of $BiVO_4$ and $Co_2P_2O_7/BiVO_4$ photoanodes under AM 1.5 G. **d** M-S curves of $BiVO_4$ and $Co_2P_2O_7/BiVO_4$ measured in the dark

charge transfer resistance (R_{ct}) of $BiVO_4$ in the Faraday impedance model [47]. To better understand the utilization efficiency of $Co_2P_2O_7/BiVO_4$ photoanode for simulated sunlight (AM 1.5 G), incident photon to current efficiency (IPCE, Fig. 5b) and applied bias photon to current efficiency (ABPE, Fig. 5c) measurements were carried out. $Co_2P_2O_7/BiVO_4$ has an IPCE value of up to 58.7% at 430 nm, nearly 2.8 times higher than that of $BiVO_4$ (21.2%). The ABPE of $Co_2P_2O_7/BiVO_4$ also reaches a maximum (1.24%) at 0.75 V vs. RHE, which is nearly 5.5 times higher than the maximum ABPE (0.23%) of $BiVO_4$. Thus, the results revealed that $Co_2P_2O_7$ ultrathin nanosheets could greatly improve the utilization and conversion efficiency of $BiVO_4$ for visible light by promoting the surface reaction kinetics and carrier transfer of $BiVO_4$. The Mott Schottky (M-S) measurements are shown in Fig. 5d. Since the tangents of the M-S curves of $Co_2P_2O_7/BiVO_4$ and $BiVO_4$ have the same intercept to the x-axis, they both have almost the same flat-band potential, indicating that the $Co_2P_2O_7$ nanosheets have less influence on the conduction band of $BiVO_4$. Meanwhile, based on the M-S plot, $Co_2P_2O_7/BiVO_4$ has a smaller slope compared with $BiVO_4$, implying that $Co_2P_2O_7/BiVO_4$ has a higher carrier density and the $Co_2P_2O_7$ ultrathin nanosheets have improved the interfacial conductivity of $BiVO_4$ [47].

To further investigate the mechanism underlying the enhanced PEC properties of $BiVO_4$ by $Co_2P_2O_7$ nanosheets, the charge injection efficiency (η_{in}, Fig. 6a) of electrolytes and charge separation efficiency (η_{sep}, Fig. 6b) were obtained by using 1 M Na_2SO_3 as a hole scavenger. Na_2SO_3 can act as a very efficient hole acceptor in the electrolyte, producing extremely fast oxidation kinetics on the surface of $BiVO_4$ and neglecting the resulting surface electron–hole recombination [12]. Hence, the photocurrent density of $BiVO_4$ and $Co_2P_2O_7/BiVO_4$ measured when 1 M Na_2SO_3 is present in the measurement electrolyte ($J_{sulfite}$, Fig. S8) should therefore represent the maximum photocurrent density when ignoring the kinetic resistance to water oxidation. The charge injection efficiency can be understood as the photocurrent density in the presence of kinetic resistance divided by the photocurrent density in the absence of kinetic resistance. The η_{in} value of $Co_2P_2O_7/BiVO_4$ at 1.23 V vs. RHE is 71%, which is equivalent to 3.5 times that of $BiVO_4$, implying that the ultrathin $Co_2P_2O_7$ nanosheets act as an extremely active OEC layer. Moreover, the η_{sep} value is defined by dividing the photocurrent density when ignoring the kinetic resistance to water oxidation by the maximum photocurrent density achieved when the photon already absorbed is fully utilized by the photoanode [48], and the η_{sep} value for $Co_2P_2O_7/BiVO_4$ at 1.23 V (vs. RHE) reaches 75%, compared to merely 65% for $BiVO_4$. When the effect of the $BiVO_4$ surface kinetic rate is negligible, the effect on its own PEC properties after coating the $BiVO_4$ surface with $Co_2P_2O_7$ can only be attributed to the $Co_2P_2O_7/BiVO_4$ junction. Therefore, any difference between the two η_{sep} values should be attributed to

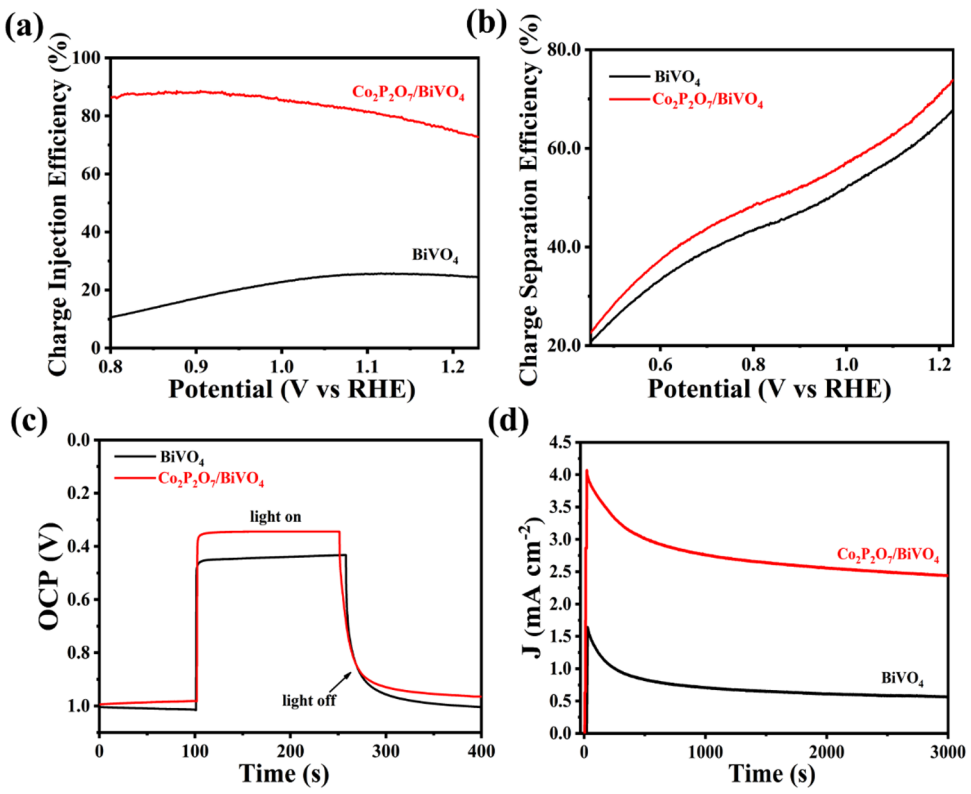

Fig. 6 **a** Charge injection efficiency and **b** charge separation efficiency of the $BiVO_4$ and $Co_2P_2O_7/BiVO_4$. **c** OCP of $BiVO_4$ and $Co_2P_2O_7/BiVO_4$ under AM 1.5 G illumination and darkness in 1 M KBi. **d** Long-term I-t curve for $Co_2P_2O_7/BiVO_4$ and $BiVO_4$, measured at 1.23 V vs. RHE

the $Co_2P_2O_7/BiVO_4$ junction, indicating that $Co_2P_2O_7$ simultaneously promotes the transfer of photogenerated holes and suppresses photogenerated electron–hole recombination at the $Co_2P_2O_7/BiVO_4$ junction [13]. In addition, we measured and compared the Open-circuit photovoltage (OCP) of $BiVO_4$ and $Co_2P_2O_7/BiVO_4$ (Fig. 6c). The OCP value of the photoanode is the open-circuit voltage under illumination minus the open-circuit voltage in the dark, caused by the splitting of the electron and hole quasi-Fermi energy levels under illumination [47]. When in open circuit voltage, no Faradaic current (redox reaction current) passes through, so kinetic effects are excluded. The increase in OCP observed after the introduction of the $Co_2P_2O_7$ nanosheet suggests a higher hole concentration at the $Co_2P_2O_7/BiVO_4$ junction, again implying that the $Co_2P_2O_7$ nanosheet inhibits charge recombination at the $Co_2P_2O_7/BiVO_4$ junction.

The stability of $Co_2P_2O_7/BiVO_4$ for PEC water splitting was also an important item to evaluate. Figure 6d shows the long-term I-t curves of $Co_2P_2O_7/BiVO_4$ and $BiVO_4$. $Co_2P_2O_7/BiVO_4$ maintains an average photocurrent density of about 70% in 3000 s.

Based on all the above discussion, we have made a hypothesis on the mechanism by which ultrathin $Co_2P_2O_7$ nanosheets can enhance the PEC water oxidation of $BiVO_4$ photoanodes. Photons with energy greater than the band gap of $BiVO_4$ are captured and converted into photogenerated hole-electron pairs within the bulk phase of $BiVO_4$. When holes are further transferred to the surface of $BiVO_4$ through the valence band, the slow charge transfer in the water oxidation kinetics will hinder the consumption of photogenerated holes and cause the accumulation and recombination of large numbers of holes on the surface (Fig. 7a). The coating of ultrathin cobalt pyrophosphate nanosheets provided an efficient transport channel to facilitate hole transfer at the $Co_2P_2O_7/BiVO_4$ junction, reducing the carrier recombination rate at this junction. Subsequently, the Co^{2+} in $Co_2P_2O_7$ receives the holes, and by virtue of the inherent OER activity of the cobalt pyrophosphate material [36] along with the high distribution density of cobalt active sites exposed in the two-dimensional morphology, $Co_2P_2O_7$ greatly accelerates the oxidation of water by photogenerated holes. The rapid water oxidation in turn promotes the hole consumption rate and further accelerates the total hole transfer process on the $BiVO_4$ surface (Fig. 7b). Meanwhile, in the system used to evaluate the properties of photoanode PEC alone, photogenerated electrons in the conduction band of $BiVO_4$ are transferred across the FTO to the Pt sheet to participate in the generation of hydrogen (Fig. 7c).

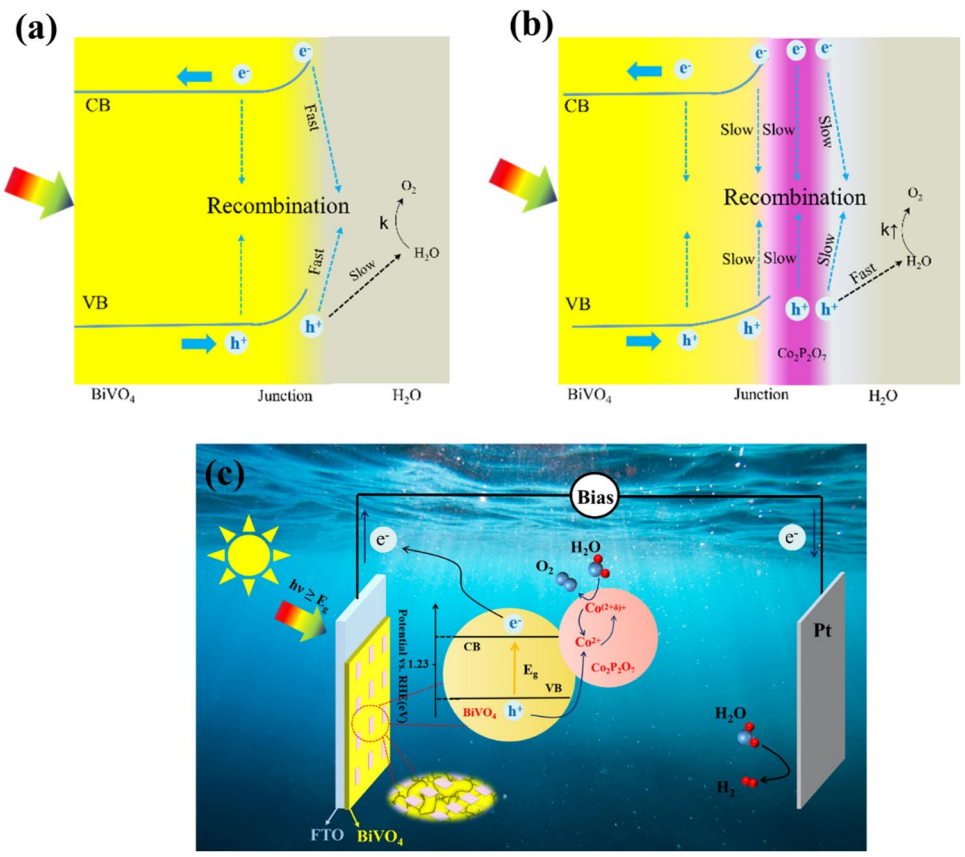

Fig. 7 **a** Illustrations of the charge transfer process for $BiVO_4$ and **b, c** $Co_2P_2O_7/BiVO_4$

4 Conclusions

In summary, we have prepared $Co_2P_2O_7/BiVO_4$ composite high-efficiency photoanodes in a facile manner. The photocurrent density under simulated solar radiation (AM 1.5 G) achieves 3.93 mA cm^{-2} (1.23 V vs. RHE) with a maximum ABPE value enhancement of nearly 5.5 times compared to that of bare $BiVO_4$. Compared to the increase in interfacial resistance caused by the introduction of ultrathin $Co_2P_2O_7$ nanosheets, their excellent carrier transport properties more importantly facilitate the transfer of photogenerated holes at the $Co_2P_2O_7/BiVO_4$ junction and avoid the creation of a large number of carrier recombination centres. The high specific surface area of $Co_2P_2O_7$ nanosheets provides a high density of cobalt active centres to receive the photogenerated holes transferred from $BiVO_4$ and to efficiently catalyse the subsequent OER of water splitting with the unique ligand environment within the $Co_2P_2O_7$ structure. This work provides an innovation in the design of cobalt-based and two-dimensional cocatalysts to enhance the PEC performance of $BiVO_4$ photoanodes.

Supplementary Information The online version contains supplementary material available at https://doi.org/10.1007/s10562-023-04293-3.

Funding This work was financially supported by the National Natural Science Foundation of China (22278345) and the Key Scientific Research Fund of Hunan Provincial Education Department (21A0089).

Declarations

Conflict of interest The authors declare that they have no conflict of interest.

References

1. Walter MG, Warren EL, McKone JR, Boettcher SW, Mi QX, Santori EA, Lewis NS (2010) Chem Rev 110:6446–6473
2. Moniz SJA, Zhu J, Tang JW (2014) Adv Energy Mater 4:1301590
3. Yu Q, Meng XG, Wang T, Li P, Ye JH (2015) Adv Func Mater 25:2686–2692
4. Lu Y, Yang YL, Fan XY, Li YQ, Zhou DH, Cai B, Wang LY, Fan K, Zhang K (2022) Adv Mater 34:2108178
5. Qi Y, Zhang JW, Kong Y, Zhao Y, Chen SS, Li D, Liu W, Chen YF, Xie TF, Cui JY, Li C, Domen K, Zhang FX (2022). Nat Commun 13:484. https://doi.org/10.1038/s41467-022-28146-6
6. Lee BR, Lee MG, Park H, Lee TH, Lee SA, Bhat SSM, Kim C, Lee S, Jang HW (2019) ACS Appl Mater Interfaces 11:20004–20012
7. Khoomortezaei S, Abdizadeh H, Golobostanfard MR (2019) ACS Appl Energy Mater 2:6428–6439
8. Pihosh Y, Minegishi T, Nandal V, Higashi T, Katayama M, Yamada T, Sasaki Y, Seki K, Suzuki Y, Nakabayashi M, Sugiyamaa M, Domen K (2020) Energy Environ Sci 13:1519–1530
9. Xiao YQ, Feng C, Fu J, Wang FZ, Li CL, Kunzelmann VF, Jiang CM, Nakabayashi M, Shibata N, Sharp ID, Domen K, Li YB (2020) Nat Catal 3:932–940
10. Chen D, Liu ZF, Zhang SC (2020) Appl Catal B-Environ 265:118580
11. Wang T, Long XF, Wei SQ, Wang P, Wang CL, Jin J, Hu GW (2020) ACS Appl Mater Interfaces 12:49705–49712
12. Lee DK, Lee D, Lumley MA, Choi K-S (2019) Chem Soc Rev 48:2126–2157
13. Kim TW, Choi KS (2014) Science 343:990–994
14. Kim JH, Lee JS (2019) Adv Mater 31:1806938
15. Lee DK, Choi KS (2018) Nat Energy 3:53–60
16. Pilli SK, Furtak TE, Brown LD, Deutsch TG, Turner JA, Herring AM (2011) Energy Environ Sci 4:5028–5034
17. Wang YX, Chen DM, Zhang JN, Balogun MS, Wang PS, Tong YX, Huang YC (2022) Adv Funct Mater 32:2112738
18. Wang GM, Ling YX, Lu XH, Qian F, Tong YX, Zhang JZ, Lordi V, Leao CR, Li Y (2013) J Phys Chem C 117:10957–10964
19. Wang SC, Chen P, Bai Y, Yun JH, Liu G, Wang LZ (2018) Adv Mater 30:1800486
20. Zhang BB, Wang L, Zhang YJ, Ding Y, Bi YP (2018) Angew Chem-Int Ed 57:2248–2252
21. Chang XX, Wang T, Zhang P, Zhang JJ, Li A, Gong JL (2015) J Am Chem Soc 137:8356–8359
22. Bai SL, Han JY, Zhang KW, Zhao YY, Luo RX, Li DQ, Chen AF (2022) Int J Hydrogen Energy 47:4375–4385
23. Zhong DK, Choi S, Gamelin DR (2011) J Am Chem Soc 133:18370–18377
24. Yan D, Fu X, Shang Z, Liu J, Luo H (2019) Chem Eng J 361:853–861
25. Zhou S, Chen K, Huang J, Wang L, Zhang M, Bai B, Liu H, Wang Q (2020) Appl Catal B-Environ 266:118513
26. Tan CL, Cao XH, Wu XJ, He QY, Yang J, Zhang X, Chen JZ, Zhao W, Han SK, Nam GH, Sindoro M, Zhang H (2017) Chem Rev 117:6225–6331
27. Song YR, Zhang XM, Zhang YX, Zhai PL, Li ZW, Jin DF, Cao JQ, Wang C, Zhang B, Gao JF, Sun LC, Hou JG (2022) Angew Chem-Int Ed 61. https://doi.org/10.1002/ange.202200946
28. Liu P, Yi J, Bao R, Zhao H (2022) Mater Today Chem 23:100747
29. Shi L, Xu CL, Jiang DX, Sun X, Wang XP, Wang QC, Zhang YL, Qu XF, Du FL (2019) Nanotechnology 30:075601
30. He WH, Wang RR, Zhang L, Zhu J, Xiang X, Li F (2015) J Mater Chem A 3:17977–17982
31. Luo L, Wang ZJ, Xiang X, Yan DP, Ye JH (2020) ACS Catal 10:4906–4913
32. Nan F, Cai TY, Ju S, Fang L (2018) Appl Phys Lett 112:173902
33. Li B, Gu P, Feng YC, Zhang GX, Huang KS, Xue HG, Pang H (2017) Adv Funct Mater 27:1605784
34. Zhao S, Wang Y, Dong J, He C-T, Yin H, An P, Zhao K, Zhang X, Gao C, Zhang L, Lv J, Wang J, Zhang J, Khattak AM, Khan NA, Wei Z, Zhang J, Liu S, Zhao H, Tang Z (2016) Nat Energy 1:16184
35. Tang FM, Cheng WR, Su H, Zhao X, Liu QH (2018) ACS Appl Mater Interfaces 10:6228–6234
36. Kim H, Park J, Park I, Jin K, Jerng SE, Kim SH, Nam KT, Kang K (2015) Nat Commun 6:8253
37. Chang YX, Shi NE, Zhao SL, Xu DD, Liu CY, Tang YJ, Dai ZH, Lan YQ, Han M, Bao JC (2016) ACS Appl Mater Interfaces 8:22534–22544
38. Du HF, Ai W, Zhao ZL, Chen Y, Xu X, Zou CJ, Wu LS, Su L, Nan KK, Yu T, Li CM (2018) Small 14:1801068
39. Li B, Zhu RM, Xue HG, Xu Q, Pang H (2020) J Colloid Interface Sci 563:328–335
40. Huang JW, Tian Y, Wang YN, Liu TT (2021) J Solid State Chem 299:122154
41. Du JY, Zhong XH, He HC, Huang J, Yang MJ, Ke GL, Wang J, Zhou Y, Dong FQ, Ren Q, Bian L (2018) ACS Appl Mater Interfaces 10:42207–42216

42. Yaw CS, Ruan QS, Tang JW, Soh AK, Chong MN (2019) Chem Eng J 364:177–185
43. Wang QZ, He JJ, Shi YBA, Zhang SL, Niu TJ, She HD, Bi YP, Lei ZQ (2017) Appl Catal B-Environ 214:158–167
44. Tang YQ, Wang RR, Yang Y, Yan DP, Xiang X (2016) ACS Appl Mater Interfaces 8:19446–19455
45. Wang YZ, Kong MG, Liu ZW, Lin CC, Zeng Y (2017) J Mater Chem A 5:24269–24274
46. Wang SC, He TW, Yun JH, Hu YX, Xiao M, Du AJ, Wang LZ (2018) Adv Funct Mater 28:1802685
47. Pan JB, Wang BH, Wang JB, Ding HZ, Zhou W, Liu X, Zhang JR, Shen S, Guo JK, Chen L, Au CT, Jiang LL, Yin SF (2021) Angew Chem-Int Ed 60:1433–1440
48. Kim TW, Ping Y, Galli GA, Choi KS (2015) Nat Commun 6:8769

Publisher's Note Springer Nature remains neutral with regard to jurisdictional claims in published maps and institutional affiliations.

Springer Nature or its licensor (e.g. a society or other partner) holds exclusive rights to this article under a publishing agreement with the author(s) or other rightsholder(s); author self-archiving of the accepted manuscript version of this article is solely governed by the terms of such publishing agreement and applicable law.